The wave-driven current in coastal canopies

Maryam Abdolahpour,[1,2] Magnus Hambleton,[1] and Marco Ghisalberti[1,3]

Corresponding author: M. Abdolahpour, School of Civil, Environmental and Mining Engineering, University of Western Australia (M015), 135 Stirling Highway, Perth, WA 6009, Australia. (maryam.abdolahpour@uwa.edu.au)

[1]School of Civil, Environmental and Mining Engineering, University of Western Australia, Perth, WA 6009, Australia

[2]School of Natural Sciences, Edith Cowan University, Joondalup, WA 6027, Australia

[3]Department of Infrastructure Engineering, University of Melbourne, Parkville, VIC 3010, Australia

Key Points.

- Wave-driven flows over a canopy generate a strong mean current which can be up to 75% of the RMS orbital velocity far above the canopy.
- The strength of this current, which is centered near the top of the canopy, increases with vertical orbital excursion and canopy density.
- The characterization of the mean current presented here will allow an enhanced capacity for the description of canopy residence time in wave-dominated systems.

Abstract. Wave-driven flows over canopies of aquatic vegetation (such as seagrass) are characterized by the generation of a strong, shoreward mean current near the top of the canopy. This shoreward drift, which is observed to be up to 75% of the RMS above-canopy orbital velocity, can have a significant impact on residence times within coastal canopies. There have been limited observations of this current and an accurate formulation of its magnitude is still lacking. Accordingly, this study aims to develop a practical relationship to describe the strength of this current as a function of both wave and canopy characteristics. A simple model for the Lagrangian drift velocity indicates that the magnitude of the wave-driven current increases with the above-canopy oscillatory velocity, the vertical orbital excursion at the top of the canopy and the canopy density. An extensive laboratory study, using both rigid and (dynamically-scaled) flexible model vegetation, was carried out to evaluate the proposed model. Experimental results reveal a strong agreement between predicted and measured current velocities over a wide and realistic range of canopy and wave conditions. The validity of this model is also confirmed through available field measurements. Characterization of

this wave-induced mean current will allow an enhanced capacity for predicting residence time, and thus key ecological processes, in coastal canopies.

1. Introduction

Rough benthic boundaries are ubiquitous in the coastal environment and include a multitude of ecologically-important aquatic ecosystems, such as seagrass meadows [*Duarte*, 2002], coral reefs [*Monismith*, 2007] and kelp forests [*Rosman et al.*, 2007]. The drag exerted by these coastal canopies reduces the near-bed velocity and attenuates wave energy [*Kobayashi et al.*, 1993; *Manca et al.*, 2012; *Maza et al.*, 2015]. This, in turn, promotes sedimentation [*Gacia et al.*, 1999], carbon burial [*Granata et al.*, 2001] and retention of particulate material [*Fonseca and Cahalan*, 1992; *Granata et al.*, 2001; *French*, 2006]. Thus, besides providing food and shelter for a range of species [*Gambi et al.*, 1990; *Koch et al.*, 2006], aquatic canopies can enhance light penetration and promote productivity [*Gruber and Kemp*, 2010; *Gruber et al.*, 2011]. In addition, aquatic canopies play an essential role in regulating water quality through the direct uptake of nutrients and dissolved organic matter [*Moore*, 2004; *Larkum et al.*, 2006] as well as the production of oxygen [*Carpenter and Lodge*, 1986; *Larkum et al.*, 2006].

The capacity of an aquatic canopy to provide these ecosystem services is tightly limited by the exchange of water across canopy boundaries [*Duarte*, 1995]. Rapid exchange also has a tremendous impact on particle mobility [*Palmer et al.*, 2004], including the transport of pollen [*Ackerman*, 1997, 2002; *Dupont et al.*, 2006] and dispersal of seeds [*Orth et al.*, 1994]. It may also prevent coral bleaching [*Nakamura and Van Woesik*, 2001] and the loss of symbiotic algae from the tissue of the coral polyps [*Hoegh-Guldberg*, 1999]. Therefore, the ecological health and propagation and environmental influence of coastal canopies

depends largely on the exchange, and thus residence time, of dissolved and particulate materials in these systems.

In coastal canopy environments, the impact of advection on residence time is often neglected [*Abdolahpour et al.*, 2017]. Although coastal systems are typically wave-dominated, this impact may not, however, necessarily be small. Indeed, aquatic canopies in oscillatory flows have been shown to generate a strong, shoreward mean current near the canopy-water interface [*Luhar et al.*, 2010]. This shoreward drift, which has been observed in both laboratory [*Lowe et al.*, 2005a; *Luhar et al.*, 2010] and field studies [*Luhar et al.*, 2013], can significantly influence canopy residence time by introducing a second method of water renewal (other than vertical mixing across the top of the canopy).

This mean current can also substantially modify the posture of flexible canopy, as shown in Figure 1. The shoreward current creates a more pronated canopy in the direction of wave propagation under the wave crest (Figure 1a) and a more upright posture under the wave trough (Figure 1b). This modification of canopy posture can impact several important canopy-element-scale processes such as photosynthesis [*Zimmerman*, 2003], nutrient uptake [*Hurd*, 2000] and oxygen transfer [*Mass et al.*, 2010]. Moreover, the drag reduction caused by the reconfiguration of flexible canopies can greatly diminish wave attenuation [*Maza et al.*, 2015]. Extreme canopy pronation (under, for example, storm conditions) can also increase the rate of stem fracture along the line of weakness, resulting in plant loss and further reduced wave attenuation [*Möller et al.*, 2014].

In coastal systems, vertical gradients in oscillatory velocity are known to drive mean currents, including the Stokes drift near the surface [*Dean and Dalrymple*, 1991; *Nielsen*, 1992] and boundary layer streaming near the bed [*Fredsøe and Deigaard*, 1992]. Al-

though Stokes drift is the manifestation of open orbits of fluid particles, boundary layer streaming is believed to be a consequence of a shear-induced non-zero temporal correlation of horizontal and vertical oscillatory velocities, which creates a wave stress near the bed [*Scandura*, 2007; *Kranenburg et al.*, 2012]. For laminar flow over a flat bed, this results in a shoreward mean current within the boundary layer [*Longuet-Higgins*, 1953].

In coastal canopy flows, the drag exerted by the canopy results in a vertical gradient of orbital velocity across the canopy-water interface. That is, the velocity within the canopy, U_c^{rms} (where the superscript 'rms' refers to the root-mean-square of the oscillatory velocity and the subscript 'c' to the in-canopy average), is attenuated from its value far above the canopy, U_∞^{rms} (Figure 2). This velocity attenuation, which is greater for denser canopies [*Lowe et al.*, 2005b; *Reidenbach et al.*, 2007; *Pujol et al.*, 2013], creates a shear layer across the top of the canopy (as seen in steady flows).

Previous research has hypothesized that velocity shear near the canopy top is the source of the shoreward mean current in coastal canopies through a mechanism analogous to boundary layer streaming [*Luhar et al.*, 2010, 2013]. By quantifying the wave Reynolds stress set up by a submerged canopy, and balancing that against canopy drag, *Luhar et al.* [2010] established a theoretical model for the mean drift within the canopy:

$$\overline{u}_c = \sqrt{\frac{4}{3\pi}\frac{C_{Dw}}{C_{Dc}}\frac{k}{\omega}{U_c}^3} \tag{1}$$

where $\overline{u}_c$ is the vertically-averaged in-canopy mean current, C_{Dw} and C_{Dc} are the time-varying and steady components of the drag coefficient (respectively), k is the wavenumber, ω is the wave radian frequency and U_c is the amplitude of the in-canopy oscillatory velocity.

It was assumed that U_c is equal to the near-bed velocity amplitude in the absence of the canopy (U_b), which can be predicted from linear wave theory:

$$U_b = \frac{H\omega}{2\sinh kh} \tag{2}$$

where H is the wave height and h is the water depth. For simplicity, C_{Dw}/C_{Dc} was assumed to be one. Generally, reasonable agreement was observed between the formulation in (1) and laboratory measurements when the RMS horizontal orbital excursion above the canopy ($A_\infty^{rms} = U_\infty^{rms}/\omega$) exceeded the stem-to-stem distance of canopy elements (S) [*Luhar et al.*, 2010]. The model underpredicts (by a factor of nearly 3) the mean current generated in the field during periods of strong waves [see field measurements by *Luhar et al.*, 2013]; an improvement is achieved in subsequent work when a time-varying frontal area of the flexible canopy is introduced [*Luhar et al.*, 2013].

Despite the reasonable agreement between model and experiment, the impact of canopy density is absent from the formulation in (1), meaning that is likely valid over only a limited range of coastal canopies. We hypothesize here that any roughness-driven current must be dependent upon the density of the canopy. Accordingly, as a step towards improving estimation of canopy residence time, this study aims to use wave flume experiments to develop an alternate model for the strength of mean currents generated in wave-dominated flows over submerged canopies across a wide and realistic range of canopy and wave conditions. Note that, although we focus here on seagrass meadows as the archetypal coastal canopy, the results of this study will be equally applicable to a wide range of marine canopies formed by, for example, coral or kelp.

2. Model development

In the absence of a canopy, fluid particles under a small-amplitude wave have sinusoidally-varying velocities with closed elliptical trajectories (Figure 3a). However, the near-surface vertical gradient in orbital velocity causes fluid particles to travel faster in the direction of wave propagation at the top of their orbit than in the opposite direction at the bottom of their orbit. This leads to open particle orbits and a time-averaged mean current (the Stokes drift) in the direction of wave propagation [*Nielsen*, 1992; *Kundu and Cohen*, 1990].

In the presence of a submerged canopy, a similar vertical velocity gradient is generated near the canopy-water interface (Figure 2). As the Lagrangian view in Figure 3a illustrates, this will result in open particle orbits and a Lagrangian mean current in the direction of wave propagation that is analogous to Stokes drift, albeit with a different underlying cause [*Jacobsen*, 2016]. Importantly, this drift is manifest in fixed-point velocity records (as seen for Stokes drift [*Umeyama*, 2010, 2012]), as oscillating fluid particles move with the drift during their shoreward motion and against it during their seaward motion. Thus, the oscillatory velocity amplitude is enhanced in the onshore direction and reduced in the offshore direction, leading to a non-zero measured mean velocity (Figure 3b). The vertical profile of mean velocity ($\overline{u}$) for a typical wave ($T = 5$ s and $U_{\infty}^{rms} = 19$ cm/s) along with the horizontal velocity signals at the top of, and far above, the canopy, clearly show the oscillatory velocity asymmetry resulting from this mechanism (Figure 3b).

It is expected that the strength of the mean current at any given height will be directly proportional to the maximum velocity difference experienced by fluid particles whose orbits encompass that height. We assume that the maximum velocity, $\overline{u}_{max}$, occurs at the

top of the canopy (where the shear is greatest) and since all fluid particles whose orbits encompass this height remain within $\pm\xi_T$ of the canopy top (where ξ_T is the total vertical orbital excursion at the top of the canopy), it is expected that:

$$\overline{u}_{max} \sim \delta U \tag{3}$$

where

$$\delta U = u^{rms}_{(h_c+\xi_T)} - u^{rms}_{(h_c-\xi_T)} \tag{4}$$

Denoting z as the vertical direction (positive upward, with $z = 0$ at the bed) and h_c as the canopy height, $u^{rms}_{(h_c+\xi_T)}$ and $u^{rms}_{(h_c-\xi_T)}$ are the RMS oscillatory velocities at $z = h_c + \xi_T$ and $z = h_c - \xi_T$, respectively.

The velocity difference introduced in (3), δU, can not be readily predicted, particularly for flexible canopies. We expect δU to depend upon (i) the vertical orbital excursion at the top of the canopy ξ_T, and (ii) the vertical gradient in oscillatory velocity set up by the canopy drag. The magnitude of this velocity gradient depends upon the characteristic velocity far above the canopy, U^{rms}_{∞}, and the canopy drag, which is indicated by its drag length scale, L_D [*Abdolahpour et al.*, 2017]:

$$L_D = \frac{1 - \lambda_p}{C_D a} \tag{5}$$

Here, λ_p is the solid fraction of the canopy, a is the canopy frontal area per unit volume and C_D is the canopy drag coefficient. So, it is expected that

$$\overline{u}_{max} \sim \delta U = f(U^{rms}_{\infty}, \xi_T, L_D) \tag{6}$$

A simple dimensional reasoning solution to (6) is:

$$\frac{\overline{u}_{max}}{U_{\infty}^{rms}} = f\left(\frac{\xi_T}{L_D}\right) \tag{7}$$

To develop a predictive formulation for $\overline{u}_{max}$, the functional form of (7) will be determined using experimental data.

3. Methods

3.1. Experimental setup

Experiments were conducted in a 50-m-long, 1.2-m-deep and 1.2-m-wide wave flume (Figure 4) with a still water depth (h) of 0.76 m. The wave flume was equipped with a programmable piston-type wave generator located in the middle of the flume. Wooden beaches of slope 1 : 10 were installed at both ends of the flume. The beaches were covered with rubber mats at the front and less porous Polyetherane filter foam at the back so that incident waves encountered regions of progressively decreasing porosity. The beach length exceeded the incident wavelength in all experiments. The reflection coefficient in the flume was estimated by measuring wave height along a transect parallel to the direction of wave propagation, with the difference between the maximum and minimum wave heights along the transect used to quantify reflection [see *Abdolahpour et al.*, 2017, for more detail]. For wave conditions typical of this study, the reflection coefficient of the flume varied from $2 - 10\%$. This level of reflection, while causing slight spatial variation in local wave heights and orbital velocities, has invariably been deemed negligible in previous studies investigating the generation of time-averaged currents under waves [e.g. *Sleath*, 1985; *Villaret and Perrier*, 1992; *Luhar et al.*, 2010; *Umeyama*, 2012].

3.2. Model vegetation

Two types of model canopy, rigid and flexible, were used in this study. Rigid model canopies can successfully capture the salient features of vegetated flow hydrodynamics, and permit a canopy geometry that is invariant and easily quantified [e.g. *Seginer et al.*, 1976; *Raupach et al.*, 1986; *Lowe et al.*, 2005b]. They also faithfully represent canopies of hard corals. Rigid canopies in these experiments consisted of 30-cm-long wooden dowels (with a diameter d of 6.4 mm) affixed to perforated PVC boards (Figure 5a).

Given that many coastal canopies (e.g. seagrasses, kelps and soft corals) exhibit significant flexibility, it is important to develop a formulation for the wave-driven current that also applies to flexible canopies. Accordingly, flexible model canopies (Figure 5b) were designed to mimic the bladed seagrass species *Posidonia australis*. Faithful recreation of canopy motion relies on matching two dimensionless force ratios that govern plant dynamics. The first ratio is that of the buoyancy force on a blade, F_B, to the restoring force on the blade due to its rigidity, F_R:

$$B = \frac{F_B}{F_R} \sim \frac{(\rho_w - \rho_s) g h_b^3}{E t^2} \tag{8}$$

[*Ghisalberti and Nepf*, 2002; *Luhar and Nepf*, 2011]. Here, ρ_w and ρ_s are the densities of water and seagrass, respectively, t is the blade thickness, h_b is the blade height and E is the modulus of elasticity, which describes the resistance of the blade to deformation. Blades with low values of B exhibit cantilever-like motion, while those with higher values exhibit a more 'whip-like' motion [*Ghisalberti and Nepf*, 2002]. The second dimensionless ratio, the Cauchy number (Ca), represents the ratio of the drag force on the blade, F_D, to the restoring force:

$$Ca = \frac{F_D}{F_R} \sim \frac{\rho_w C_D (U_c^{rms})^2 h_b^3}{E t^3}, \tag{9}$$

where U_c^{rms} is the RMS in-canopy oscillatory velocity (Figure 2). The Cauchy number defines the mean pronation of the canopy, which increases with Ca [*Luhar and Nepf*, 2011, 2015]. Estimation of C_D for coastal canopies is difficult as it varies significantly with canopy and wave properties. Previous studies, however, suggest as reasonable a value of $C_D \simeq 1$ for the waves and canopies employed in this study [see e.g. *Mendez and Losada*, 2004; *Anagnostopoulos and Dikarou*, 2012; *Jadhav et al.*, 2013].

Trial model blades with $0.04 < B < 0.4$ were constructed from Low Density Polyethylene (LDPE). These trial plants, along with a typical, real *Posidonia australis* leaf, were then subjected to different wave conditions to determine, visually (matching Ca), the model blade that exhibited the most realistic plant motion. Blades with $B = 0.085$ (corresponding to a 30 cm length, 1 cm width (b) and 300 μm thickness), exhibited the most realistic behavior across all wave phases. Note that B was chosen as the primary matching parameter between the model and real plant as Ca is not constant and depends heavily on flow conditions. To mimic *Posidonia australis*, which is characterized by two or three differently-sized blades on each stem [*Kuo*, 1978], each model plant was constructed from two blades (with heights 15 and 30 cm) of this width and thickness. The model blades were attached to a 3-cm wooden dowel to represent the stiffness of the *Posidonia australis* stem (Figure 5b). While embedding flexibility and vertical variation in frontal area allows for a more realistic representation of coastal canopies, the model canopies have a uniform composition. Natural benthic environments may, however, exhibit a more diverse composition, potentially of both rigid and flexible species [*Weitzman et al.*, 2015]. In these

multispecific systems, a single value of flexibility (and, indeed, canopy height) may not accurately characterize the entire canopy.

Three rigid canopies with dimensionless frontal area $ad = 0.016$, 0.063 and 0.131 (denoted as RL, RM and RH hereafter) were employed (Table 1). In the flexible canopies, as each canopy element consisted of two blades of differing heights, the canopy frontal area varied over depth. We therefore describe flexible canopies through their vertically-averaged dimensionless frontal area ab_{eff} (Figure 6). Note that ab_{eff} is the dimensionless frontal area of the canopy based on the full blade height and width (i.e. for the canopy being completely upright and perpendicular to the flow). Two flexible canopies with $ab_{eff} = 0.064$ and 0.145 (denoted as FM and FH hereafter), were used. The ranges of ad $(0.016 - 0.131)$ and ab_{eff} $(0.064 - 0.145)$ employed here (Table 1) span typical densities of coastal canopies [*Gambi et al.*, 1990; *Luhar et al.*, 2010].

The canopy height ($h_c = 30$ cm) and stem diameter for rigid canopies ($d = 0.64$ cm), the blade height ($h_b = 30$ cm) and width for flexible canopies ($b = 1$ cm) as well as water depth ($h = 0.76$ m) were kept constant throughout the experiments. The canopy length (l) was varied inversely with the canopy density (ranging from 3-9 m, Table 1). To minimize edge effects, the length of the canopy on either side of the measurement location was at least four times the total horizontal orbital excursion far above the canopy.

Each canopy was exposed to up to nineteen flow conditions by varying the wave period ($T = 5 - 9$ s) and above canopy RMS velocity ($U_\infty^{rms} = 3.0 - 21.5$ cm/s) (Table 2). All generated waves were shallow-water waves with $kh \leqslant 0.35$ [*Dean and Dalrymple*, 1991], typical of coastal seagrass meadows [*Koch et al.*, 2006].

3.3. Velocity measurements

Vertical profiles of velocity were taken in the middle of the canopy using an Acoustic Doppler Velocimeter (ADV). In rigid canopies, data points were spaced every 2 cm; in flexible canopies, velocity data were taken every 1 cm for $z < 16$ cm, and every 2 cm for $z \geq 16$ cm to focus on the near-bed region where the velocity gradient was expected to be greatest.

In dense rigid canopies (i.e. RM and RH), a small area (of $\sim$ 5-cm diameter) was cleared of dowels to allow ADV access into the canopy (Figure 4). It was observed here that the larger clearing required to allow ADV access inside flexible canopies [e.g. *Neumeier and Ciavola*, 2004; *Pujol et al.*, 2010] significantly altered the magnitude of RMS velocities and mean current near the top of the canopy (by up to 30% and 20%, respectively). Therefore, the flexible canopies were not modified; instead, ADV data inside the canopy that were contaminated by model blades entering the sampling volume (as indicated by beam correlations $< 70\%$) were excluded from analysis. The excluded data points were distributed quasi-randomly throughout the wave cycle, such that data exclusion did not significantly bias the estimated flow statistics. The extent of data exclusion was small with less than 1% of the data excluded in nearly all records. Figure 7a shows a typical profile of RMS velocities (Run 18-FM in Table 1) obtained from raw and filtered data. Filtering the data does not significantly alter the estimates of U_∞^{rms} (Figure 7a) and current speed (Figure 7b). It does, however, impact RMS velocity estimates in the vicinity of the top of the canopy, but this is not critical to the analysis presented here. Filtered data were therefore used for all flexible canopies in this study.

Data were recorded at 25 Hz in all profiles. For rigid canopies, a sampling time of 6 minutes (40-70 wave cycles) was employed; for flexible canopies, this was increased to 10 minutes (70-120 wave cycles) to allow for data removal. Analysis of long velocity records within and above these canopies demonstrated convergence of flow statistics at these sampling times.

To investigate the lateral variation of the flow structure, velocity profiles were taken at two distances from the side-walls (20 cm and 50 cm) in Run 16-RM. The currents generated at the top of the canopy differed by less than 5%, such that the lateral variation of the flow was assumed to be negligible in these experiments.

Velocity statistics were obtained through phase-averaging. The phase angle (φ, from -π to π) of each velocity data point was determined through a Hilbert transform. Data were then grouped into a minimum of 91 phase bins, with each bin containing at least 100 data points. At any given height, the root-mean-square (RMS) of the oscillatory velocity in the direction of wave propagation, U^{rms}, was calculated according to:

$$U^{rms} = \sqrt{\frac{1}{2\pi}\int_{-\pi}^{\pi} \left(\langle u\left(\varphi\right)\rangle - \overline{u}\right)^2 d\varphi} \tag{10}$$

where the angular brackets represent the phase average over several wave periods.

3.4. Vertical orbital excursion

The vertical orbital excursion at the top of the canopy (ξ_T) was calculated according to linear wave theory:

$$\xi_T = \frac{H}{2}\frac{\sinh(kh_c)}{\sinh(kh)}. \tag{11}$$

[*Dean and Dalrymple*, 1991]. For flexible canopies, the vertical orbital excursion was evaluated at the top of the canopy in its fully upright position (i.e. at $z = 30$ cm). For the shallow-water waves examined here, the estimation of ξ_T will not be markedly sensitive to this choice of canopy height. However, for deep-water waves, where the vertical excursion varies more dramatically over depth, the model accuracy may be more sensitive to the point at which the vertical excursion is evaluated. In practice, it is more common to measure wave height, rather than ξ_T; the two are related simply according to Equation 11.

4. Results

The maximum current speed in the profile ($\overline{u}_{max}$) for every combination of wave and canopy characteristics is presented in Table 2. Values of A_∞^{rms}/S exceeded 1 for all runs (for both rigid and flexible canopies).

It is important to note that, in a closed system, mean currents are generated even in the absence of a submerged canopy. For waves with $kh \ll 1$ (as in this study), a current in the direction of wave propagation is generated near the bed, with a weaker backward drift above (see *Longuet-Higgins* [1953]). This velocity structure is demonstrated in Figure 8, where the observed vertical profile of mean velocity ($\overline{u}$) in the absence of a canopy shows good qualitative agreement with the prediction of *Longuet-Higgins* [1953] for a wave with $kh = 0.35$ and $U_\infty^{rms} = 19$ cm/s. For comparison, the observed profile of $\overline{u}$ for an identical wave over a rigid canopy with $ad = 0.063$ (Run 16-RM) is also displayed. Through conservation of mass, the strong current at the top of the canopy creates compensating return flows in the offshore direction. The presence of this return flow can attenuate the strength of the measured current ($\overline{u}_{max}$). By assuming a return flow that is uniformly distributed through the water column, the magnitude of the return flow in this study is

low, ranging from $6 - 20\%$ of $\overline{u}_{max}$. Thus, the closed nature of the flume may induce discrepancies (relative to open systems) of this order. The time-averaged velocity near the canopy top exceeds the velocity in the absence of the canopy by at least an order of magnitude, implying that the closed nature of the wave flume negligibly impacts the currents generated at the top of the experimental canopies. Through conservation of mass, the strong current at the top of the canopy creates weak compensating return flows well above and below the canopy shear layer in the closed experimental system (Figure 8).

4.1. Variation of $\overline{u}$

As expected, larger waves generate stronger mean currents over a given canopy (Figure 9a). More importantly, the magnitude of this mean current increases with canopy density for a given wave condition (Figure 9b). This highlights a limitation of the formulation in (1), which does not contain a dependence on canopy density.

As previously discussed, we expect $\overline{u}$ to attain a maximum value near the top of the canopy, where the shear is strongest. The experimental results presented in Figure 9 strongly support this for both rigid and flexible vegetation. The height of a flexible canopy oscillates throughout the wave cycle. As a result, a more diffuse peak in the profile of mean velocity is observed over flexible canopies (Figure 9c); this peak velocity is centered around the top of the canopy under maximum pronation.

Figure 9 highlights the strength of this mean current and its potential role in driving advective flushing of coastal canopies. The magnitude of $\bar{u}_{max}/U_{\infty}^{rms}$ is as high as 50% for the canopy and wave conditions presented in Figure 9 and takes a maximum value of 75% in this study (Run 12-FH, Table 2).

4.2. Prediction of wave-driven mean current

Equation (1) does not accurately predict the magnitude of the currents observed here (Figure 10). The observed depth-averaged current inside the canopy ($\overline{u}_c$) is plotted against the Equation (1) prediction for the flexible canopies of this study (given that the formulation was initially tested on data from flexible canopies). In Figure 10a, the amplitude of the in-canopy oscillatory velocity, U_c, is estimated from linear wave theory assuming no velocity attenuation by the canopy (i.e. $U_c \equiv U_b$ in Equation (2), as per *Luhar et al.* [2010]); in Figure 10b, the measured value of U_c in these experiments is used. While both definitions of U_c provide reasonably accurate predictions of the depth-averaged current speed in the experiments of *Luhar et al.* [2010], neither one allows accurate predictions within the comparatively dense canopies studied here. The clear relationship between canopy density and current strength (Figure 9b) means that Equation (1) cannot provide accurate estimates across the range of densities of real coastal canopies; as shown in Figure 10b, the model clearly underpredicts the current strength for dense canopies. Thus, it is imperative that a density-dependent formulation for the current strength be developed here.

We first evaluate the hypothesis that this current is driven by the velocity differential experienced by particles during their orbit. To do this, the dependence of $\overline{u}_{max}$ on the velocity difference experienced by particles at the top of the canopy (δU, Equation (4)) is examined across all runs with rigid canopies (Figure 11). The magnitude of the current is directly proportional to δU ($\mathrm{R}^2 = 0.80$) with an $O(1)$ coefficient of proportionality. This strongly supports the hypothesis underlying a model of a velocity-gradient-driven current at the canopy top.

The functional form of (7) that is best supported by the experimental data is

$$\overline{u}_{max} = 0.5\ U_{\infty}^{rms} \left(\frac{\xi_T}{L_D} \right)^{0.3} \tag{12}$$

As shown in Figure 12, there is a strong collapse ($R^2 = 0.83$) when observed current speeds are compared to Equation (12) across the range of canopies (rigid and flexible, dense and sparse) employed here. This model also demonstrates strong agreement with the experimental data of *Luhar et al.* [2010] and the field measurement of *Luhar et al.* [2013]. The good agreement between the predicted model and the field measurement (where there is no return current, as the system is open) indicates that the return flows in the laboratory were not strong enough to significantly impact the measured current. Importantly, the field measurement falls below the line of best fit. If the attenuating impact of the return flows was significant, the proposed model would significantly underestimate the wave-driven current. Given the uncertainty in estimating a and C_D, key parameters required to estimate the drag length scale of flexible canopies, the validity of (12) in describing the current generated by both rigid and flexible canopies is quite remarkable. Importantly, Equation (12) makes sound physical sense. The maximum current speed increases with the vertical orbital excursion, as particles will sample a greater velocity difference with increasing excursion. It also increases with increasing canopy density (i.e. with decreasing L_D), as denser canopies generate stronger velocity gradients.

4.3. Advective flux

4.3.1. Rigid canopies

There is a clear collapse of vertical profiles of current speed around the top of rigid canopies when the current is normalized by its maximum value ($\overline{u}_{max}$) and the vertical

scale is normalized by the vertical orbital excursion, ξ_T (Figure 13). The scatter of data in the upper regions of the water column (i.e. above the shear layer) is likely due to the compensating return flow generated in the closed system. Due to canopy resistance, this compensating flow is preferentially diverted above the canopy (as seen in Figures 8 and 9). It is noteworthy that the significant mean current is confined to one vertical orbital excursion above and below the canopy-water interface; i.e. $-1 < (z - h_c)/\xi_T < 1$ (Figure 13). This further supports the model developed in Section 2 (Figure 3), where only particles whose orbits span the shear layer at the canopy top experience the Lagrangian drift. The region of non-zero shoreward velocity (highlighted in Figure 13) extends slightly higher than this, however. This is because the shear layer that forms at the top of the canopy is (a) of non-zero thickness, and (b) is centered above the canopy top. Therefore, fluid particles that sample a gradient in oscillatory velocity in their orbits (and thus experience a shoreward drift) can exist above $z = h_c + \xi_T$. The region of non-zero shoreward velocity indeed extends above this point (Figure 13).

Guided by the average point of zero-crossing of the mean velocity profiles, the total advective flux (q) generated by the canopy was estimated by integration of the velocity profile from $-1 < (z - h_c)/\xi_T < 2$, i.e.

$$q = \int_{h_c - \xi_T}^{h_c + 2\xi_T} \overline{u}\, dz \tag{13}$$

Given the collapse observed in Figure 13, the integral in Equation (13) scales simply on $\overline{u}_{max}\ \xi_T$, such that:

$$q = \gamma\ \overline{u}_{max}\ \xi_T \tag{14}$$

where γ is the scaling coefficient determined by experiment. There is a clear linear relationship ($R^2 = 0.86$) between the total observed advective flux in rigid canopies (q_r, calculated from (13)) and observed values of ($\overline{u}_{max}\xi_T$) (Figure 14). The coefficient of proportionality is $\gamma = 1.2$.

4.3.2. Flexible canopies

Description of the total flux for flexible canopies is challenging due to the variation of the canopy height over the wave cycle. This creates a wider vertical region within which the current is generated (Figure 15). In this figure, a constant canopy height of $h_c = 30$ cm is employed in defining the normalized vertical scale $(z - h_c)/\xi_T$, for consistency with rigid canopies. Unlike in rigid canopies, vertical profiles of the mean current do not exhibit a collapse, with the location of maximum velocity varying with wave conditions. Moreover, the maximum velocity consistently occurs at lower levels than in rigid canopies, due presumably to pronation of the canopy during the wave cycle. Notwithstanding the uncertainties associated with the time-varying canopy height, Figure 15 suggests that $\overline{u}$ contributes to the shoreward mass flux, predominantly, within a region of thickness $3\xi_T$ centered around the maximum velocity, consistent with rigid canopies. Evaluating mass flux within this region for each run results in a clear scaling of q_f (where q_f is the total advective flux in flexible canopies) on ($\overline{u}_{max}\xi_T$) (Figure 16). The coefficient of proportionality for flexible canopies is $\gamma = 1.9$. This is greater than that for rigid canopies, due to the more diffuse profile of mean velocity in flexible canopies.

The greater value of γ for flexible canopies is not unexpected, due to the asymmetry in canopy drag. In flexible canopies, fluid particles experience a lower canopy drag when moving in the shoreward direction and a greater drag when moving in the seaward direc-

tion because of the asymmetry in the plant posture through the wave cycle (Figure 1). This asymmetry will lead to an increased velocity differential experienced by fluid particles in the region of significant flow and, ultimately, a stronger mean current generation.

4.4. Implications for predicting residence time in real canopies

While Equation (12) accurately describes the Eulerian measure of the roughness-driven current, it is the Lagrangian velocity that will govern the residence time of dissolved and particulate material within the canopy. Confirmation that (12) accurately predicts total Lagrangian transport is key in moving towards predictive capability for canopy residence times.

Additionally, although creating model plants with differently-sized flexible blades allowed examination of the roughness-driven current in realistic systems, the model canopies were entirely uniform. Natural benthic environments may contain multi-specific canopies with significant intra-canopy variation in density, flexibility and elasticity, and thus pronation. Characterization of the behavior of multispecific canopies in coastal systems, and the mean currents that they generate, is a fundamentally-important research challenge. Finally, despite the good agreement between the model and the existing field measurement, the proposed model will require full validation in open coastal systems (i.e. in the absence of return flows).

5. Conclusion

Vertical gradients in oscillatory velocity across the top of submerged coastal canopies cause fluid particles located near the canopy top to move faster in the shoreward direction than in the seaward direction. This leads to a time-averaged mean velocity near the top

of the canopy in the direction of wave propagation. The maximum value of this current, $\overline{u}_{max}$, can be as much as 75% of the RMS orbital velocity far above the canopy.

In this study, a simple, practical formulation for the magnitude of this mean current is presented as a function of both wave and canopy conditions. The proposed formulation (Equation (12)), indicates that the maximum current speed ($\overline{u}_{max}$) increases with the above-canopy orbital velocity, the vertical orbital excursion at the top of the canopy and canopy density. There is good agreement between observed currents and predicted values across a wide and realistic range of wave and canopy properties (including flexibility). This model can therefore be used for an accurate estimation of advective flux, and ultimately the residence time, in coastal canopies. The total mass flux generated by this mechanism is $q \simeq 1.2\ \overline{u}_{max}\xi_T$ for rigid canopies, with a slightly enhanced value ($q \simeq 1.9\ \overline{u}_{max}\xi_T$) for flexible canopies. Characterization of this wave-induced mean current will allow an enhanced capacity for predicting residence time, and thus key ecological processes, in coastal canopies.

Acknowledgments. M. Abdolahpour gratefully acknowledges the support of a Collaborative Research Network scholarship (CRN) and a Postgraduate Research Scholarship granted by Edith Cowan University (ECUPRS) and the Australian Government. This project was funded by a grant from the Australian Department of Innovation, Industry, Science and Research's Collaborative Research Network Scheme (Grant CRN2011:05). M. Hambleton would like to thank the UWA SWANS Scholarship for providing partial funding during this study. The authors would like to thank Mitul Luhar for providing experimental data used in Figure 10, Heidi Nepf for the insightful comments on this

manuscript, and two anonymous reviewers whose comments have helped to improve this manuscript. The data presented herein are available from the first author upon request.

References

Abdolahpour, M., M. Ghisalberti, P. Lavery, and K. McMahon (2017), Vertical mixing in coastal canopies, *Limnology and Oceanography*, *62*(1), 26–42, doi:10.1002/lno.10368.

Ackerman, J. D. (1997), Submarine pollination in the marine angiosperm *Zostera marina* (zosteraceae). i. the influence of floral morphology on fluid flow, *American Journal of Botany*, *84*(8), 1099–1099.

Ackerman, J. D. (2002), Diffusivity in a marine macrophyte canopy: implications for submarine pollination and dispersal, *American Journal of Botany*, *89*(7), 1119–1127, doi:10.3732/ajb.89.7.1119.

Anagnostopoulos, P., and C. Dikarou (2012), Aperiodic phenomena in planar oscillatory flow past a square arrangement of four cylinders at low pitch ratios, *Ocean Engineering*, *52*, 91–104, doi:10.1016/j.oceaneng.2012.06.009.

Carpenter, S. R., and D. M. Lodge (1986), Effects of submersed macrophytes on ecosystem processes, *Aquatic Botany*, *26*, 341–370, doi:10.1016/0304-3770(86)90031-8.

Dean, R., and R. Dalrymple (1991), Water wave mechanics for scientists and engineers, *World Scientific, Advanced Series on Ocean Engineering*, *2*.

Duarte, C. M. (1995), Submerged aquatic vegetation in relation to different nutrient regimes, *Ophelia*, *41*(1), 87–112, doi:10.1080/00785236.1995.10422039.

Duarte, C. M. (2002), The future of seagrass meadows, *Environmental Conservation*, *29*(02), 192–206.

Dupont, S., Y. Brunet, and N. Jarosz (2006), Eulerian modelling of pollen dispersal over heterogeneous vegetation canopies, *Agricultural and Forest Meteorology*, *141*(2), 82–104, doi:10.1016/j.agrformet.2006.09.004.

Fonseca, M. S., and J. A. Cahalan (1992), A preliminary evaluation of wave attenuation by four species of seagrass, *Estuarine, Coastal and Shelf Science*, *35*(6), 565–576, doi:10.1016/S0272-7714(05)80039-3.

Fredsøe, J., and R. Deigaard (1992), *Mechanics of coastal sediment transport*, vol. 3, World Scientific.

French, J. (2006), Tidal marsh sedimentation and resilience to environmental change: exploratory modelling of tidal, sea-level and sediment supply forcing in predominantly allochthonous systems, *Marine Geology*, *235*(1), 119–136.

Gacia, E., T. Granata, and C. Duarte (1999), An approach to measurement of particle flux and sediment retention within seagrass (*Posidonia oceanica*) meadows, *Aquatic Botany*, *65*(1), 255–268, doi:10.1016/S0304-3770(99)00044-3.

Gambi, M. C., A. R. Nowell, and P. Jumars (1990), Flume observations on flow dynamics in *Zostera marina* (eelgrass) beds, *Marine Ecology Progress Series. Oldendorf*, *61*(1), 159–169, doi:10.3354/meps061159.

Ghisalberti, M., and H. M. Nepf (2002), Mixing layers and coherent structures in vegetated aquatic flows, *Journal of Geophysical Research*, *107*(C2), 3011, doi:10.1029/2001JC000871.

Granata, T., T. Serra, J. Colomer, X. Casamitjana, C. Duarte, E. Gacia, and J. Petersen (2001), Flow and particle distributions in a nearshore seagrass meadow before and after a storm, *Marine Ecology Progress Series*, *218*, 95–106, doi:10.3354/meps218095.

Gruber, R. K., and W. M. Kemp (2010), Feedback effects in a coastal canopy-forming submersed plant bed, *Limnology and Oceanography*, *55*(6), 2285–2298, doi: 10.4319/lo.2010.55.6.2285.

Gruber, R. K., D. C. Hinkle, and W. M. Kemp (2011), Spatial patterns in water quality associated with submersed plant beds, *Estuaries and Coasts*, *34*(5), 961–972, doi: 10.1007/s12237-010-9368-0.

Hoegh-Guldberg, O. (1999), Climate change, coral bleaching and the future of the world's coral reefs, *Marine and Freshwater Research*, *50*(8), 839–866, doi:10.1071/MF99078.

Hurd, C. L. (2000), Water motion, marine macroalgal physiology, and production, *Journal of Phycology*, *36*(3), 453–472, doi:10.1046/j.1529-8817.2000.99139.x.

Jacobsen, N. G. (2016), Wave-averaged properties in a submerged canopy: Energy density, energy flux, radiation stresses and stokes drift, *Coastal Engineering*, *117*, 57–69.

Jadhav, R. S., Q. Chen, and J. M. Smith (2013), Spectral distribution of wave energy dissipation by salt marsh vegetation, *Coastal Engineering*, *77*, 99–107, doi: 10.1016/j.coastaleng.2013.02.013.

Kobayashi, N., A. W. Raichle, and T. Asano (1993), Wave attenuation by vegetation, *Journal of waterway, port, coastal, and ocean engineering*, *119*(1), 30–48.

Koch, E. W., L. P. Sanford, S.-N. Chen, D. J. Shafer, and J. M. Smith (2006), Waves in seagrass systems: review and technical recommendations, *Tech. rep.*, DTIC Document.

Kranenburg, W. M., J. S. Ribberink, R. E. Uittenbogaard, and S. J. Hulscher (2012), Net currents in the wave bottom boundary layer: On waveshape streaming and progressive wave streaming, *Journal of Geophysical Research: Earth Surface*, *117*(F3), doi:10.1029/2011JF002070.

Kundu, P., and L. Cohen (1990), Fluid mechanics, 638 pp, *Academic, Calif.*

Kuo, J. (1978), Morphology, anatomy and histochemistry of the australian seagrasses of the genus *Posidonia könig* (posidoniaceae). i. leaf blade and leaf sheath of posidonia australis hook f., *Aquatic Botany*, *5*, 171–190.

Larkum, A. W., R. R. J. Orth, and C. M. Duarte (2006), *Seagrasses: biology, ecology, and conservation*, Springer.

Longuet-Higgins, M. S. (1953), Mass transport in water waves, *Philosophical Transactions of the Royal Society of London. Series A, Mathematical and Physical Sciences*, *245*(903), 535–581.

Lowe, R. J., J. R. Koseff, and S. G. Monismith (2005a), Oscillatory flow through submerged canopies: 1. velocity structure, *Journal of Geophysical Research: Oceans (19782012)*, *110*(C10), doi:10.1029/2004JC002788.

Lowe, R. J., J. R. Koseff, S. G. Monismith, and J. L. Falter (2005b), Oscillatory flow through submerged canopies: 2. canopy mass transfer, *Journal of Geophysical Research: Oceans (19782012)*, *110*(C10), doi:10.1029/2004JC002789.

Luhar, M., and H. Nepf (2015), Wave-induced dynamics of flexible blades, *Journal of Fluids and Structures*, *61*, 20–41, doi:10.1016/j.jfluidstructs.2015.11.007.

Luhar, M., and H. M. Nepf (2011), Flow-induced reconfiguration of buoyant and flexible aquatic vegetation, *Limnology and Oceanography*, *56*(6), 2003, doi:10.4319/lo.2011.56.6.2003.

Luhar, M., S. Coutu, E. Infantes, S. Fox, and H. Nepf (2010), Wave-induced velocities inside a model seagrass bed, *Journal of Geophysical Research: Oceans (1978–2012)*, *115*(C12), doi:10.1029/2010JC006345.

519 Luhar, M., E. Infantes, A. Orfila, J. Terrados, and H. M. Nepf (2013), Field observations
520 of wave-induced streaming through a submerged seagrass (*Posidonia oceanica*) meadow,
521 *Journal of Geophysical Research: Oceans*, *118*(4), 1955–1968, doi:10.1002/jgrc.20162.
522 Manca, E., I. Caceres, J. Alsina, V. Stratigaki, I. Townend, and C. Amos (2012), Wave
523 energy and wave-induced flow reduction by full-scale model posidonia oceanica seagrass,
524 *Continental Shelf Research*.
525 Mass, T., A. Genin, U. Shavit, M. Grinstein, and D. Tchernov (2010), Flow enhances
526 photosynthesis in marine benthic autotrophs by increasing the efflux of oxygen from
527 the organism to the water, *Proceedings of the National Academy of Sciences*, *107*(6),
528 2527–2531, doi:10.1073/pnas.0912348107.
529 Maza, M., J. Lara, I. Losada, B. Ondiviela, J. Trinogga, and T. Bouma (2015), Large-
530 scale 3-d experiments of wave and current interaction with real vegetation. part 2:
531 experimental analysis, *Coastal Engineering*, *106*, 73–86.
532 Mendez, F. J., and I. J. Losada (2004), An empirical model to estimate the propagation
533 of random breaking and nonbreaking waves over vegetation fields, *Coastal Engineering*,
534 *51*(2), 103–118, doi:10.1016/j.coastaleng.2003.11.003.
535 Möller, I., M. Kudella, F. Rupprecht, T. Spencer, M. Paul, B. K. van Wesenbeeck,
536 G. Wolters, K. Jensen, T. J. Bouma, M. Miranda-Lange, et al. (2014), Wave attenua-
537 tion over coastal salt marshes under storm surge conditions, *Nature Geoscience*, *7*(10),
538 727–731.
539 Monismith, S. G. (2007), Hydrodynamics of coral reefs, *Annual Review of Fluid Mechan-*
540 *ics*, *39*, 37–55, doi:10.1146/annurev.fluid.38.050304.092125.

Moore, K. A. (2004), Influence of seagrasses on water quality in shallow regions of the lower chesapeake bay, *Journal of Coastal Research*, pp. 162–178, doi:10.2112/SI45-162.1.

Nakamura, T., and R. Van Woesik (2001), Water-flow rates and passive diffusion partially explain differential survival of corals during the 1998 bleaching event, *Marine Ecology Progress Series*, *212*, 301–304, doi:10.3354/meps212301.

Neumeier, U., and P. Ciavola (2004), Flow resistance and associated sedimentary processes in a spartina maritima salt-marsh, *Journal of Coastal Research*, pp. 435–447, doi:10.2112/1551-5036(2004)020[0435:FRAASP]2.0.CO;2.

Nielsen, P. (1992), *Coastal bottom boundary layers and sediment transport*, vol. 4, World Scientific.

Orth, R. J., M. Luckenbach, and K. A. Moore (1994), Seed dispersal in a marine macrophyte: implications for colonization and restoration, *Ecology*, *75*(7), 1927–1939.

Palmer, M. R., H. M. Nepf, T. J. Pettersson, and J. D. Ackerman (2004), Observations of particle capture on a cylindrical collector: Implications for particle accumulation and removal in aquatic systems, *Limnology and Oceanography*, pp. 76–85, doi:10.4319/lo.2004.49.1.0076.

Pujol, D., J. Colomer, T. Serra, and X. Casamitjana (2010), Effect of submerged aquatic vegetation on turbulence induced by an oscillating grid, *Continental Shelf Research*, *30*(9), 1019–1029, doi:10.1016/j.csr.2010.02.014.

Pujol, D., T. Serra, J. Colomer, and X. Casamitjana (2013), Flow structure in canopy models dominated by progressive waves, *Journal of Hydrology*, *486*, 281–292, doi:10.1016/j.jhydrol.2013.01.024.

563 Raupach, M., P. Coppin, and B. Legg (1986), Experiments on scalar dispersion within
564 a model plant canopy part i: The turbulence structure, *Boundary-Layer Meteorology*,
565 *35*(1-2), 21–52, doi:10.1007/BF00117300.

566 Reidenbach, M. A., J. R. Koseff, and S. G. Monismith (2007), Laboratory experiments
567 of fine-scale mixing and mass transport within a coral canopy, *Physics of Fluids*, *19*,
568 075,107, doi:10.1063/1.2752189.

569 Rosman, J. H., J. R. Koseff, S. G. Monismith, and J. Grover (2007), A field in-
570 vestigation into the effects of a kelp forest (*Macrocystis pyrifera*) on coastal hydro-
571 dynamics and transport, *Journal of Geophysical Research: Oceans*, *112*(C2), doi:
572 10.1029/2005JC003430.

573 Scandura, P. (2007), Steady streaming in a turbulent oscillating boundary layer, *Journal*
574 *of Fluid Mechanics*, *571*, 265–280, doi:10.1017/S0022112006002965.

575 Seginer, I., P. Mulhearn, E. F. Bradley, and J. Finnigan (1976), Turbulent flow in a model
576 plant canopy, *Boundary-Layer Meteorology*, *10*(4), 423–453, doi:10.1007/BF00225863.

577 Sleath, J. (1985), Measurements of mass transport over a rough bed, in *Coastal Engineer-*
578 *ing 1984*, pp. 1149–1160.

579 Umeyama, M. (2010), Coupled piv and ptv measurements of particle velocities and trajec-
580 tories for surface waves following a steady current, *Journal of Waterway, Port, Coastal,*
581 *and Ocean Engineering*, *137*(2), 85–94.

582 Umeyama, M. (2012), Eulerian–lagrangian analysis for particle velocities and trajectories
583 in a pure wave motion using particle image velocimetry, *Philosophical Transactions*
584 *of the Royal Society of London A: Mathematical, Physical and Engineering Sciences*,
585 *370*(1964), 1687–1702.

586 Villaret, C., and G. Perrier (1992), Transport of fine sand by combined waves and current:
587 An experimental study, rep, *Tech. rep.*, HE-42/92.68, Electr. de France, Chatou.
588 Weitzman, J. S., R. B. Zeller, F. I. Thomas, and J. R. Koseff (2015), The attenuation
589 of current-and wave-driven flow within submerged multispecific vegetative canopies,
590 *Limnology and Oceanography*, *60*(6), 1855–1874.
591 Zimmerman, R. C. (2003), A biooptical model of irradiance distribution and photosyn-
592 thesis in seagrass canopies, *Limnology and Oceanography*, *48*(1; Part 2), 568–585, doi:
593 10.4319/lo.2003.48.1_part_2.0568.

Figure 1. The impact of the wave-induced, shoreward mean current on a dynamically-scaled flexible canopy in the laboratory. Images show the canopy at its maximum pronation (a) in the direction of wave propagation, and (b) in the direction opposite to that of wave propagation. The presence of the mean current creates an asymmetry in canopy posture, with a greatly enhanced pronation in the direction of wave propagation.

Figure 2. The increase in attenuation of orbital velocity with density in submerged canopies. Vertical profiles of RMS velocities for identical waves ($U_{\infty}^{rms} = 17$ cm/s, Run 18 in Table 2) over a dense rigid canopy (10% by volume), a sparse rigid canopy (1% by volume) and a bare bed are presented. Values of the in-canopy RMS velocity, U_c^{rms}, and the above-canopy RMS velocity, U_{∞}^{rms}, are indicated for the dense canopy. The gray dashed line represents the top of the canopy.

Figure 3. Lagrangian and Eulerian views of the wave-induced drift over coastal canopies. (a) The deviation of particle orbits from linear wave theory (left) due to the canopy resistance. Fluid particles with a mean position at the top of the canopy will have a greater velocity in the direction of wave propagation (U_1) than in the offshore direction (U_2), generating a Lagrangian drift in the direction of wave propagation. (b) In spite of a symmetric oscillation far above the canopy ($\overline{u} \approx 0$), fluid particles within approximately one vertical orbital excursion (i.e. $\pm\xi_T$) of the top of the canopy move with the drift under a wave crest and against it under a trough. This generates an asymmetric Eulerian velocity record, such that $\overline{u} \neq 0$ near the canopy-water interface (shown for a typical wave with $T = 5$ s and $U_\infty^{rms} = 19$ cm/s; Run 16-RM).

Figure 4. Schematic view of the experimental configuration in the wave tank (not to scale). Beaches of slope 1:10 were constructed at both ends of the tank to minimize wave reflection. Velocity measurements were taken by an Acoustic Doppler Velocimeter (ADV) in the geometric center of the canopy.

Figure 5. Photographs showing the ADV probe measuring within the densest (a) rigid and (b) flexible model canopies.

Figure 6. Vertical variation of dimensionless frontal area (ab) in the model *Posidonia australis* canopy. The lower region of the canopy has a greater frontal area than the upper region. The average of the upper and lower values, ab_{eff}, was used to characterize the flexible canopies.

Figure 7. Vertical profiles of (a) U_{rms} and (b) $\overline{u}$ in Run 18−FM estimated using raw and filtered data. The shaded areas represent the top of the canopy (with spatial variability) at the point of the maximum pronation in the direction of wave propagation. Gray dashed lines indicate the maximum blade height.

Figure 8. Vertical profiles of mean velocity in the absence and presence of the canopy. The observed vertical profile of mean velocity in the absence of a canopy (gray solid line) is in good agreement with the prediction of *Longuet-Higgins* [1953]. For the same wave ($U_{\infty}^{rms} = 19$ cm/s; Run 16, Table 2) in the presence of a canopy ($ad = 0.063$), the maximum current exceeds that in the absence of the canopy by an order of magnitude, typical of all the experimental runs conducted here.

Figure 9. The impact of wave and canopy conditions on the mean current generated. (a) Identical rigid canopies ($ad = 0.063$, Table 1) subjected to different waves with U_∞^{rms} between 3 and 19 cm/s. The stronger the wave forcing, the greater the mean current. (b) Identical waves ($U_\infty^{rms} = 19$ cm/s) over different rigid canopies with ad ranging from 0.016 (L) to 0.131 (H, Table 1). Importantly, stronger currents are generated by denser canopies. (c) The maximum value of $\overline{u}$ occurs near the canopy top for both rigid and flexible canopies, which is indicated by a dashed line for the rigid canopy and a gray band (representing the range of blade heights at maximum pronation) for the flexible canopy.

Figure 10. Observed (vertical axis) and predicted (horizontal axis) values of the depth-averaged current speed in the canopy ($\overline{u}_c$) for two flexible canopy densities, $ab_{eff} = 0.064$ and 0.145 (FM and FH, Table 1). Grey dashed lines indicate $1:1$ agreement. (a) Predicted value of $\overline{u}_c$ from (1), taking $U_c \equiv U_b$ as the in-canopy oscillatory velocity amplitude (Equation (2)), and (b) using values of U_c measured in these experiments. While Equation (1) provides reasonably accurate predictions of the mean currents in the experiments of *Luhar et al.* [2010] (abbreviated as LCIFN), it fails to do so in these experiments.

Figure 11. The direct proportionality ($R^2 = 0.80$) in rigid canopies between the maximum current speed ($\overline{u}_{max}$) and the velocity differential experienced by particles that encounter the top of the canopy (δU). The dashed line represents the line of the best fit. This validates the hypothesis in (3), which underpins the model presented here for wave-generated currents.

Figure 12. The accuracy of the model developed here in predicting the maximum current, $\overline{u}_{max}$. Observed $\overline{u}_{max}$ values in both rigid and flexible canopies are in good agreement ($R^2 = 0.83$) with predicted values (from Equation (12)); the dashed line represents 1 : 1 agreement. Laboratory observations from *Luhar et al.* [2010] (only considering runs for which $A_\infty^{rms}/S < 1$) and field observations from *Luhar et al.* [2013] (abbreviated as LIOTN) are also well predicted by (12).

Figure 13. The collapse of vertical profiles of mean current speed on a normalized vertical scale ($(z-h_c)/\xi_T$) for rigid canopies with (a) $ad = 0.016$ (b) $ad = 0.063$ and (c) $ad = 0.131$. The darkness of the markers is proportional to the magnitude of U_∞^{rms} (as indicated by the colorbar). The dashed lines indicate the region within one vertical orbital excursion of the canopy top and the gray bands the range over which the total advective flux was evaluated.

Figure 14. The linear proportionality between the total flux in rigid canopies (q_r) and ($\overline{u}_{max}\ \xi_T$). The strong proportionality ($R^2 = 0.86$) validates the scaling relationship in (14) for rigid canopies. The slope of the line of best fit (dashed line) defines the scaling coefficient for rigid canopies, γ (= 1.2).

Figure 15. Profiles of $\overline{u}/\overline{u}_{max}$ for the flexible canopy FH ($ab_{eff} = 0.145$) when plotted on a normalized vertical scale ($(z-h_c)/\xi_T$). The darkness of markers is proportional to the magnitude of U_∞^{rms} (as indicated by the colorbar).

Figure 16. The linear proportionality between the total flux in flexible canopies (q_f) and ($\overline{u}_{max}\ \xi_T$). The strong proportionality ($R^2 = 0.80$) validates the scaling relationship in (14). The slope of the line of best fit (dashed line) defines the scaling coefficient for flexible canopies, γ (=1.9).

Table 1. Canopy densities employed in this study.

Canopy type	Density	ad, ab_{eff}	L_D (m)	l (m)
Rigid (R)	L (Low)	0.016	0.39	9
	M (Medium)	0.063	0.10	5
	H (High)	0.131	0.05	3
Flexible (F)	M (Medium)	0.064	0.16	6
	H (High)	0.145	0.07	6

Table 2. Wave conditions employed in this study and the observed values of $\overline{u}_{max}$ near the top of the canopy.

			$\overline{u}_{max}$ (cm/s)				
Run	T (s)	U_{∞}^{rms} (cm/s)	RL	RM	RH	FM	FH
1	9	3.0	0.56	0.95	1.15	-	-
2	9	4.4	1.14	1.59	2.18	0.64	-
3	8	5.6	0.49	2.00	2.35	2.39	3.54
4	9	5.9	1.65	2.69	3.66	-	3.19
5	6	8.2	2.07	3.35	4.68	-	4.27
6	8	7.7	1.71	3.15	3.81	2.79	5.43
7	9	7.5	2.50	3.37	3.60	-	4.20
8	8	9.8	2.63	3.19	3.51	4.36	7.22
9	6	9.4	2.83	5.40	6.86	4.87	6.90
10	9	11.4	2.35	3.98	5.52	5.21	6.25
11	5	14.9	4.25	7.60	8.01	6.61	9.40
12	9	11.3	3.65	5.00	6.16	5.40	8.51
13	8	12.1	2.95	3.68	4.83	5.19	-
14	6	15.6	4.36	7.49	5.66	6.76	10.17
15	8	14.7	2.60	4.56	-	6.17	8.91
16	5	19.0	4.45	9.41	10.30	7.25	13.40
17	6	18.8	4.67	8.95	10.99	8.36	11.83
18	8	17.0	3.29	7.10	-	7.51	9.17
19	6	21.5	4.60	9.04	11.50	-	-

Figure 1.


(a)


(b)

Figure 2.

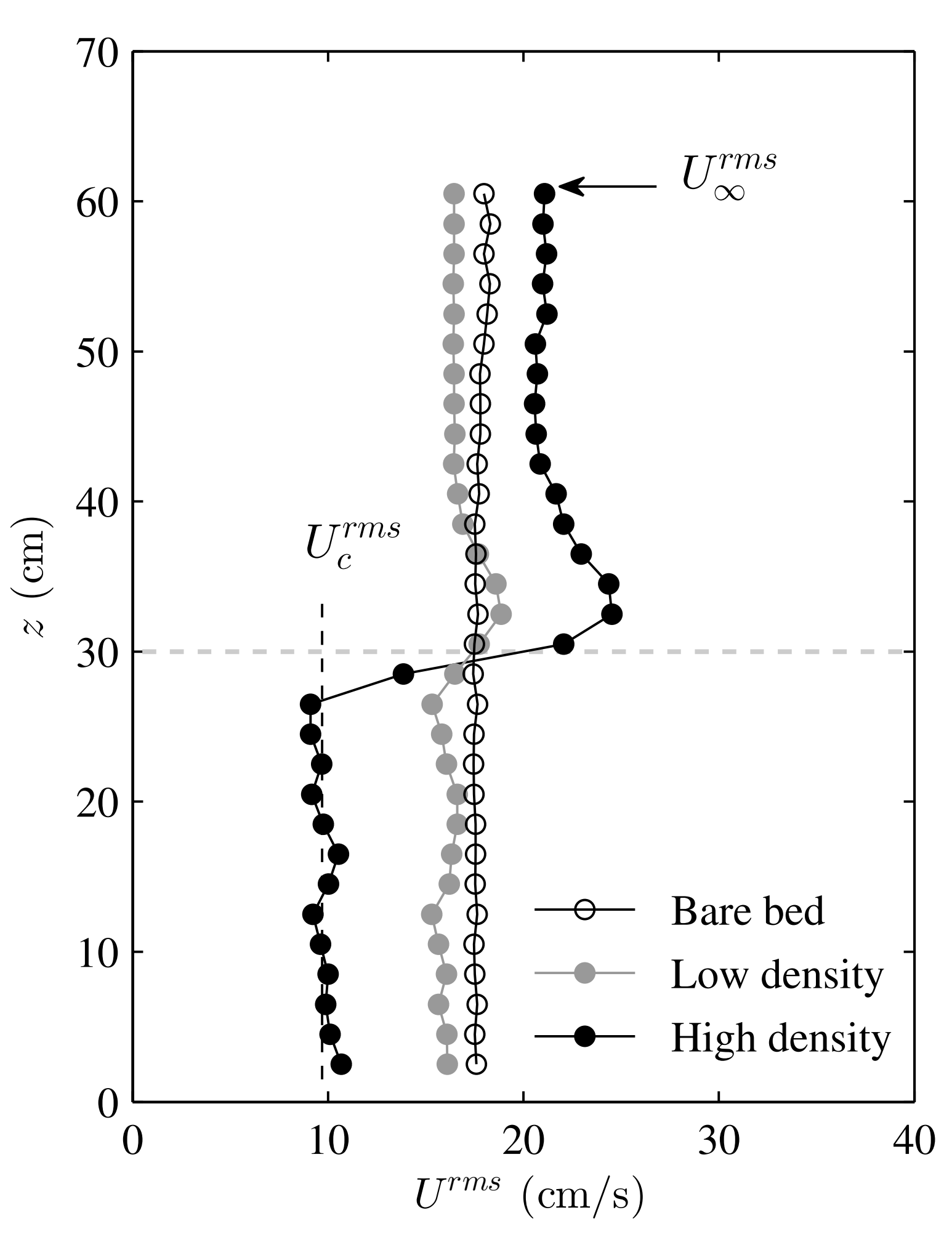
70
60
50
40
30
20
10
0
0
10
20
30
40
z (cm)
U^{rms} (cm/s)
U_∞^{rms}
U_c^{rms}
Bare bed
Low density
High density

Figure 3.

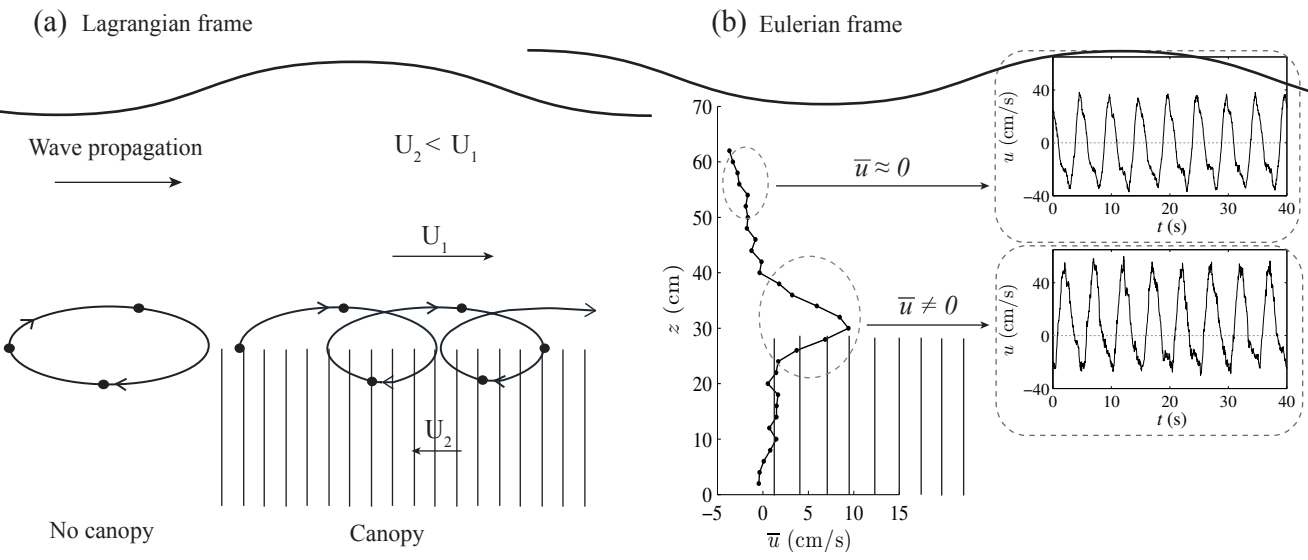
(a) Lagrangian frame
Wave propagation
$U_2 < U_1$
U_1
U_2
No canopy
Canopy
(b) Eulerian frame
$\overline{u} \approx 0$
$\overline{u} \neq 0$
z (cm)
$\overline{u}$ (cm/s)
u (cm/s)
t (s)

Figure 4.

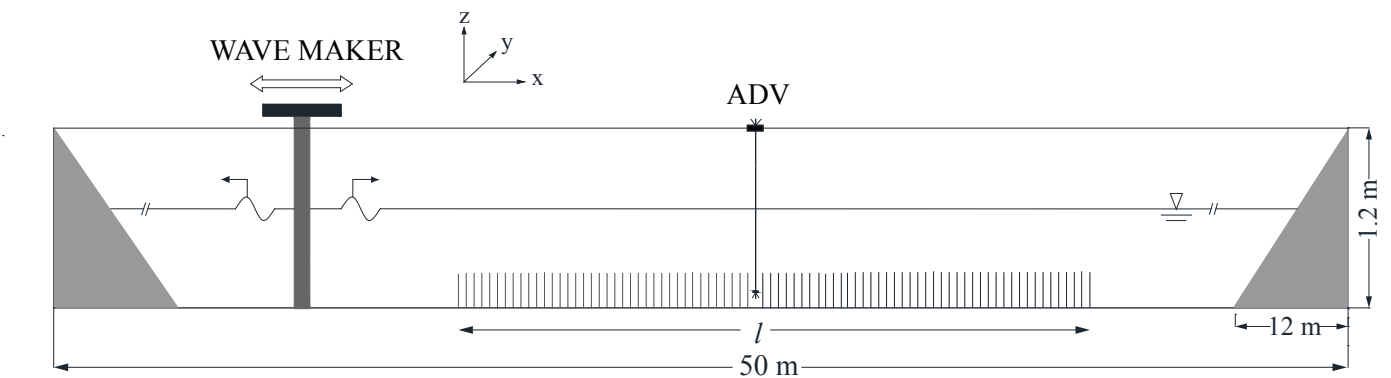
WAVE MAKER
z
y
x
ADV
1.2 m
l
12 m
50 m

Figure 5.

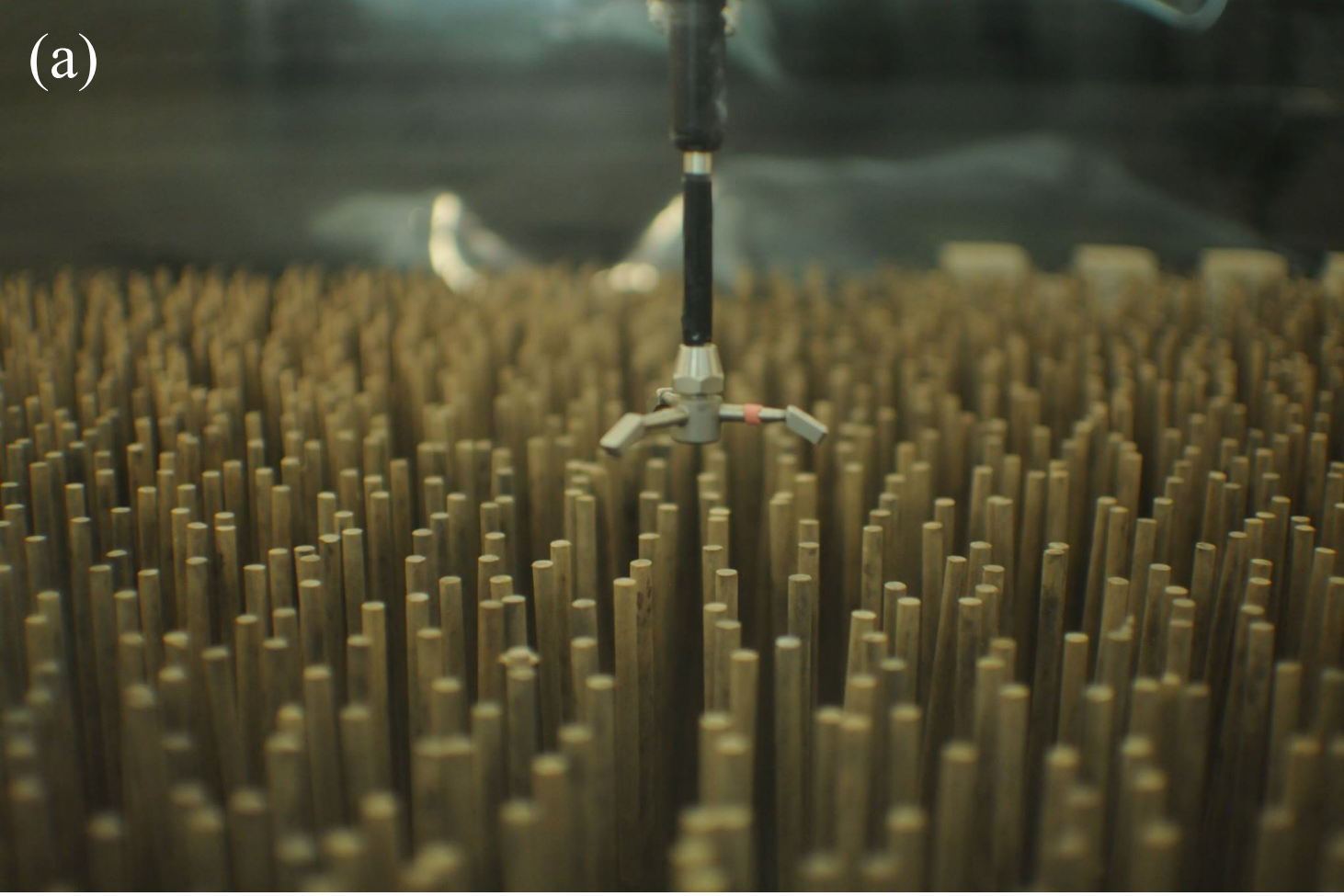
(a)


(b)

Figure 6.

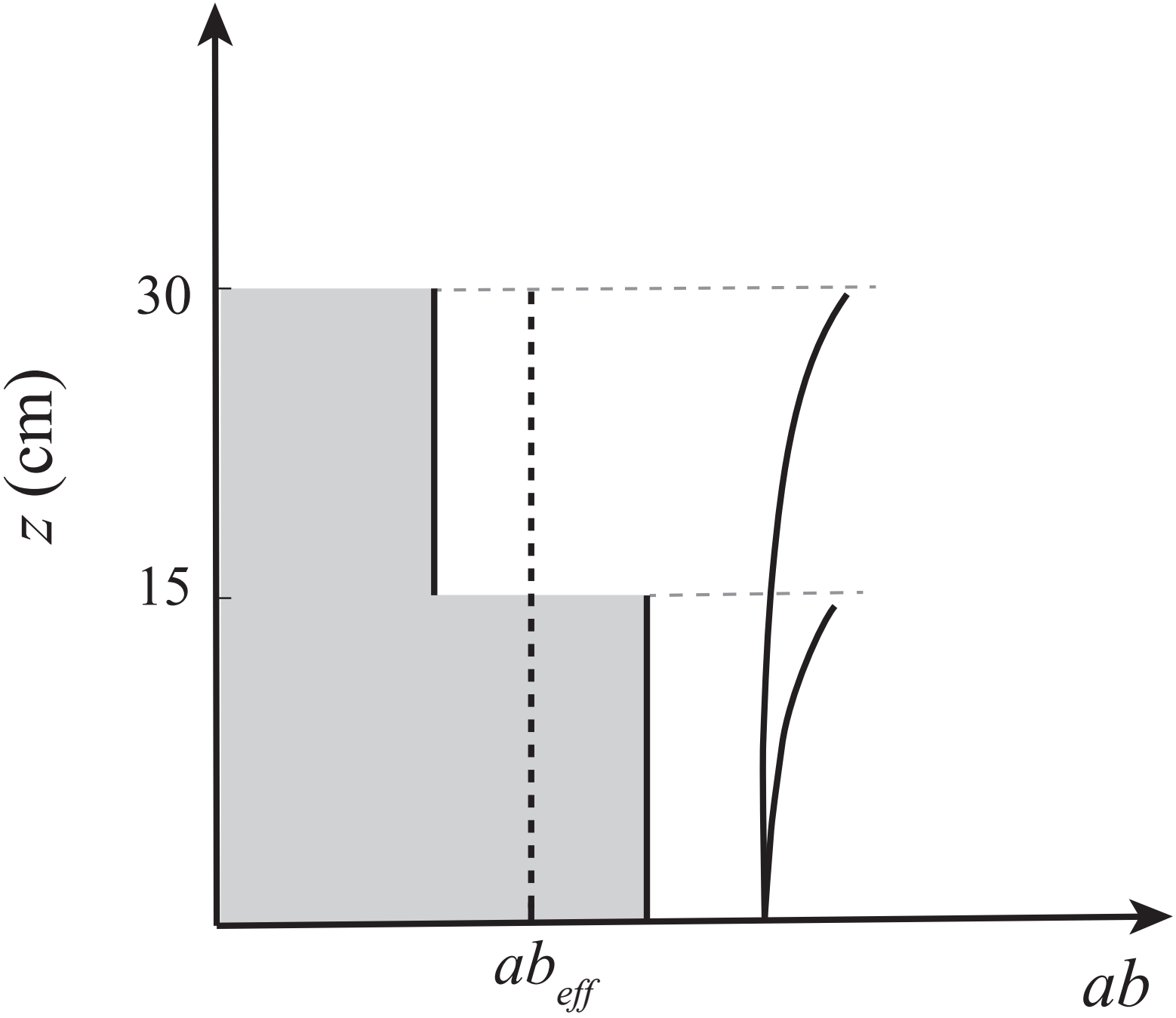
30
15
z (cm)
ab eff
ab

Figure 7.

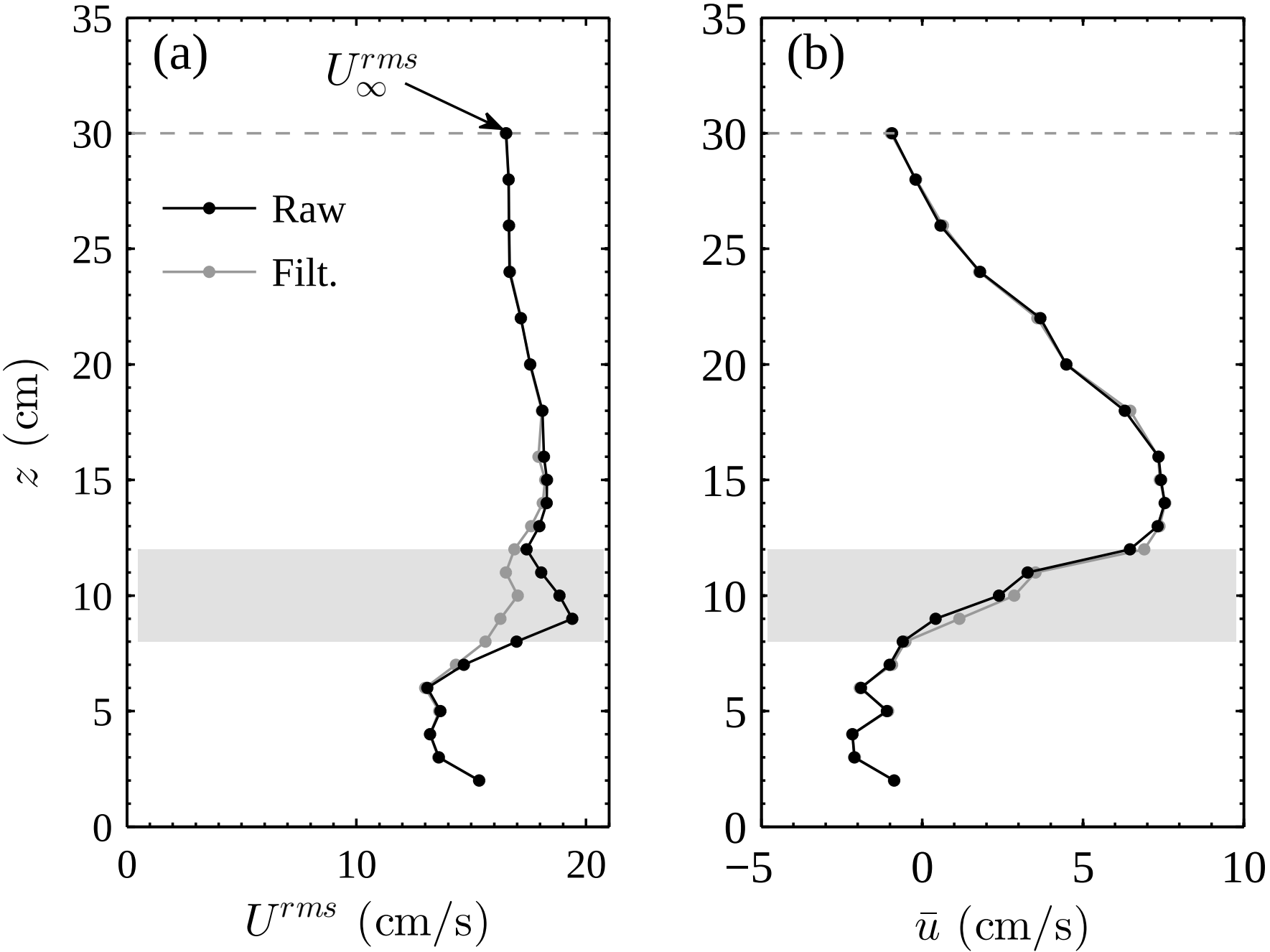
(a)
U_∞^{rms}
Raw
Filt.
z (cm)
U^{rms} (cm/s)
(b)
$\bar{u}$ (cm/s)
0
5
10
15
20
25
30
35
−5
0
5
10
20

Figure 8.

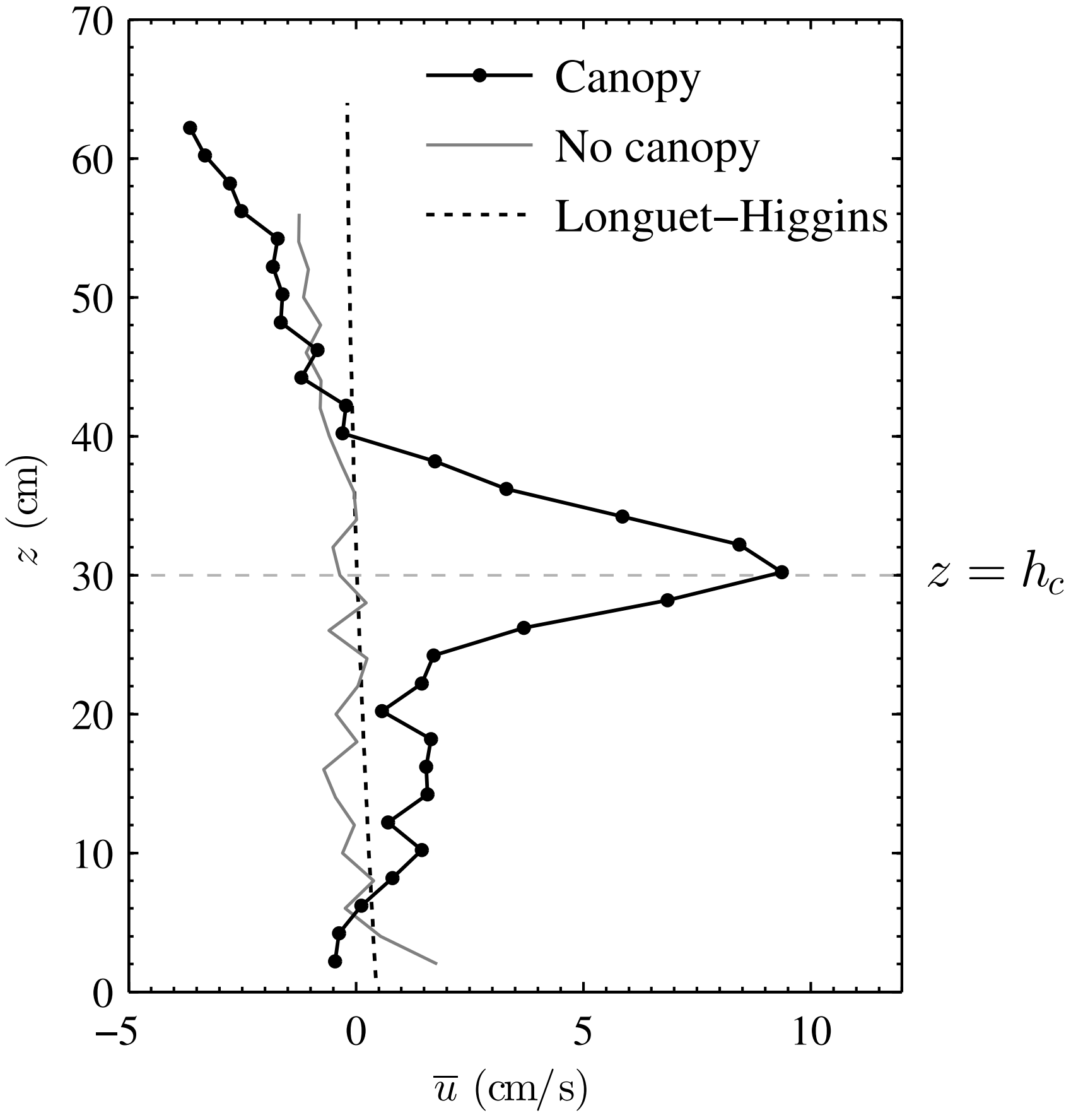
Canopy
No canopy
Longuet–Higgins
$z = h_c$
z (cm)
$\overline{u}$ (cm/s)
70
60
50
40
30
20
10
0
−5
0
5
10

Figure 9.

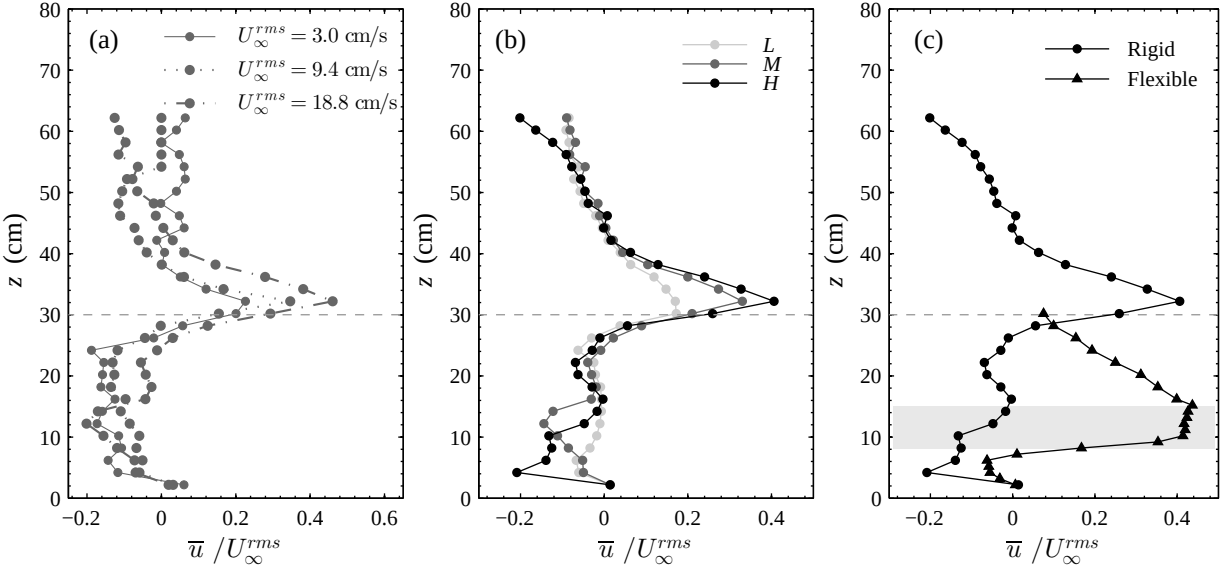
(a)
$U_\infty^{rms} = 3.0$ cm/s
$U_\infty^{rms} = 9.4$ cm/s
$U_\infty^{rms} = 18.8$ cm/s
(b)
L
M
H
(c)
Rigid
Flexible
z (cm)
$\overline{u}\ /U_\infty^{rms}$

Figure 10.

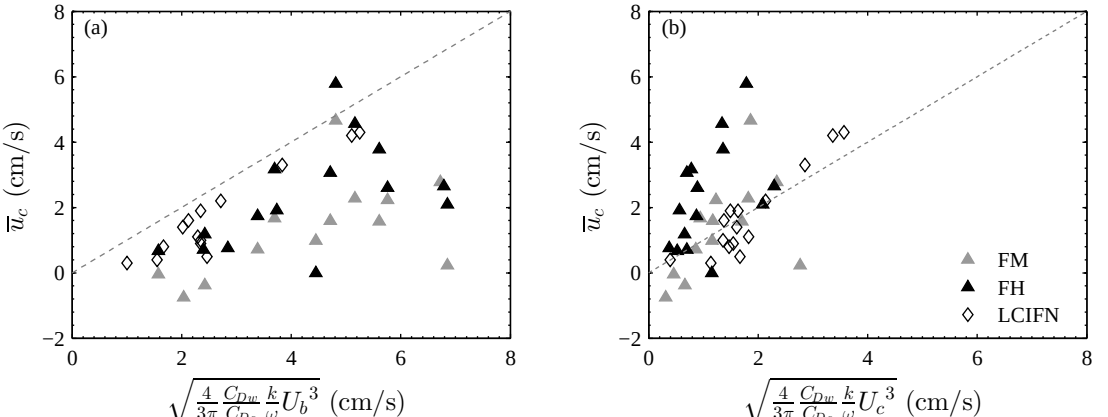
(a)
(b)
$\overline{u}_c$ (cm/s)
$\sqrt{\frac{4}{3\pi}\frac{C_{Dw}}{C_{Dc}}\frac{k}{\omega}U_b{}^3}$ (cm/s)
$\sqrt{\frac{4}{3\pi}\frac{C_{Dw}}{C_{Dc}}\frac{k}{\omega}U_c{}^3}$ (cm/s)
FM
FH
LCIFN

Figure 11.

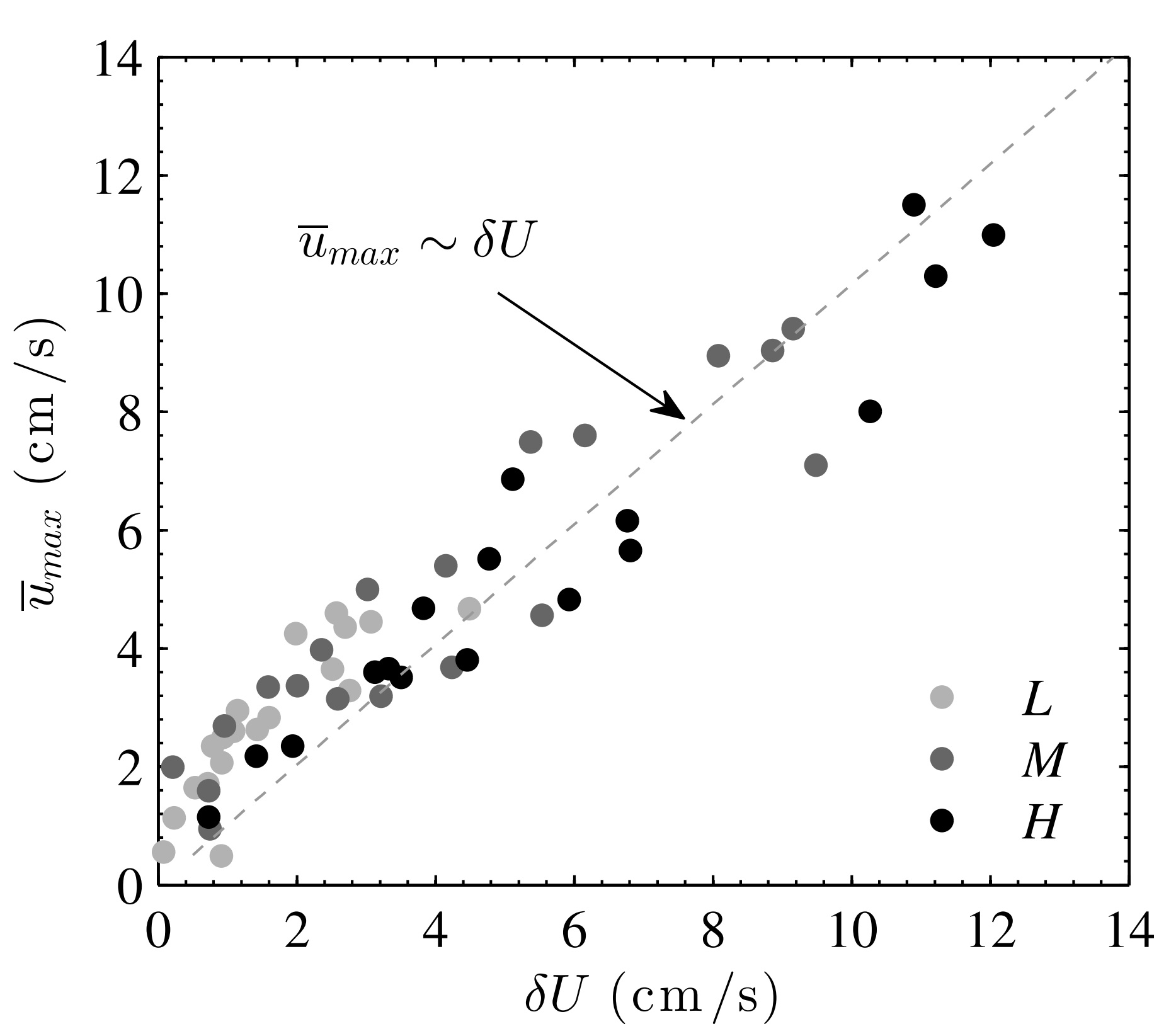
$\overline{u}_{max} \sim \delta U$
$\overline{u}_{max}$ (cm/s)
δU (cm/s)
L
M
H
0
2
4
6
8
10
12
14

Figure 12.

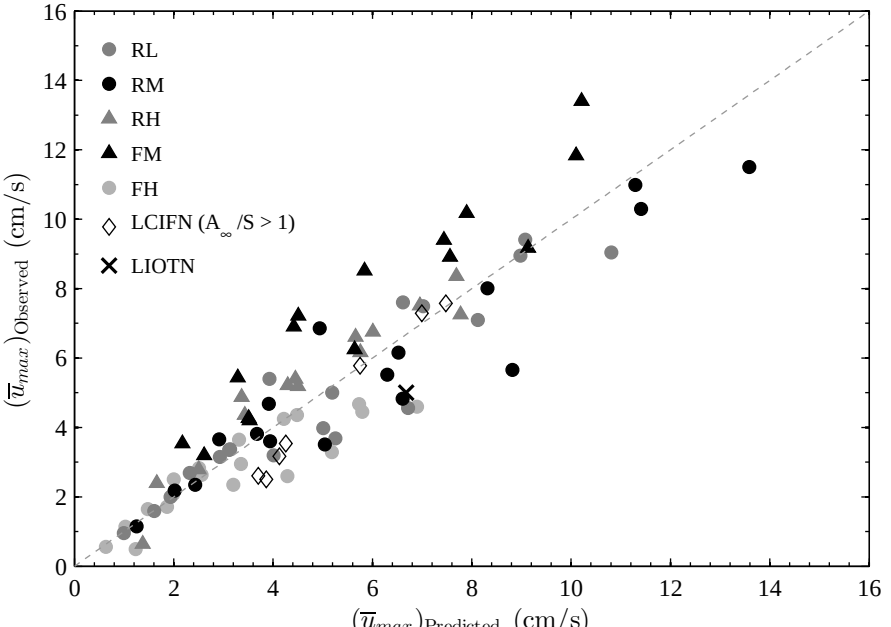
RL
RM
RH
FM
FH
LCIFN (A∞ /S > 1)
LIOTN
(u_max)Observed (cm/s)
(u_max)Predicted (cm/s)
0
2
4
6
8
10
12
14
16

Figure 13.

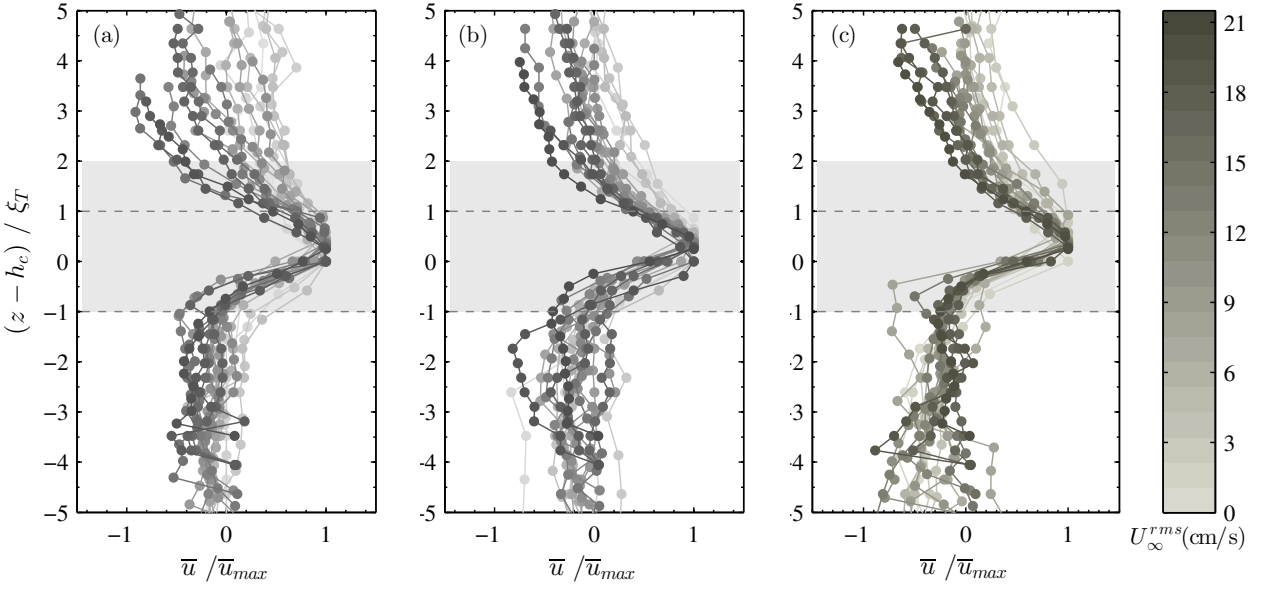
(a)
(b)
(c)
$(z - h_c) \,/\, \xi_T$
$\overline{u} \,/ \overline{u}_{max}$
$\overline{u} \,/ \overline{u}_{max}$
$\overline{u} \,/ \overline{u}_{max}$
U_∞^{rms}(cm/s)
0
3
6
9
12
15
18
21

Figure 14.

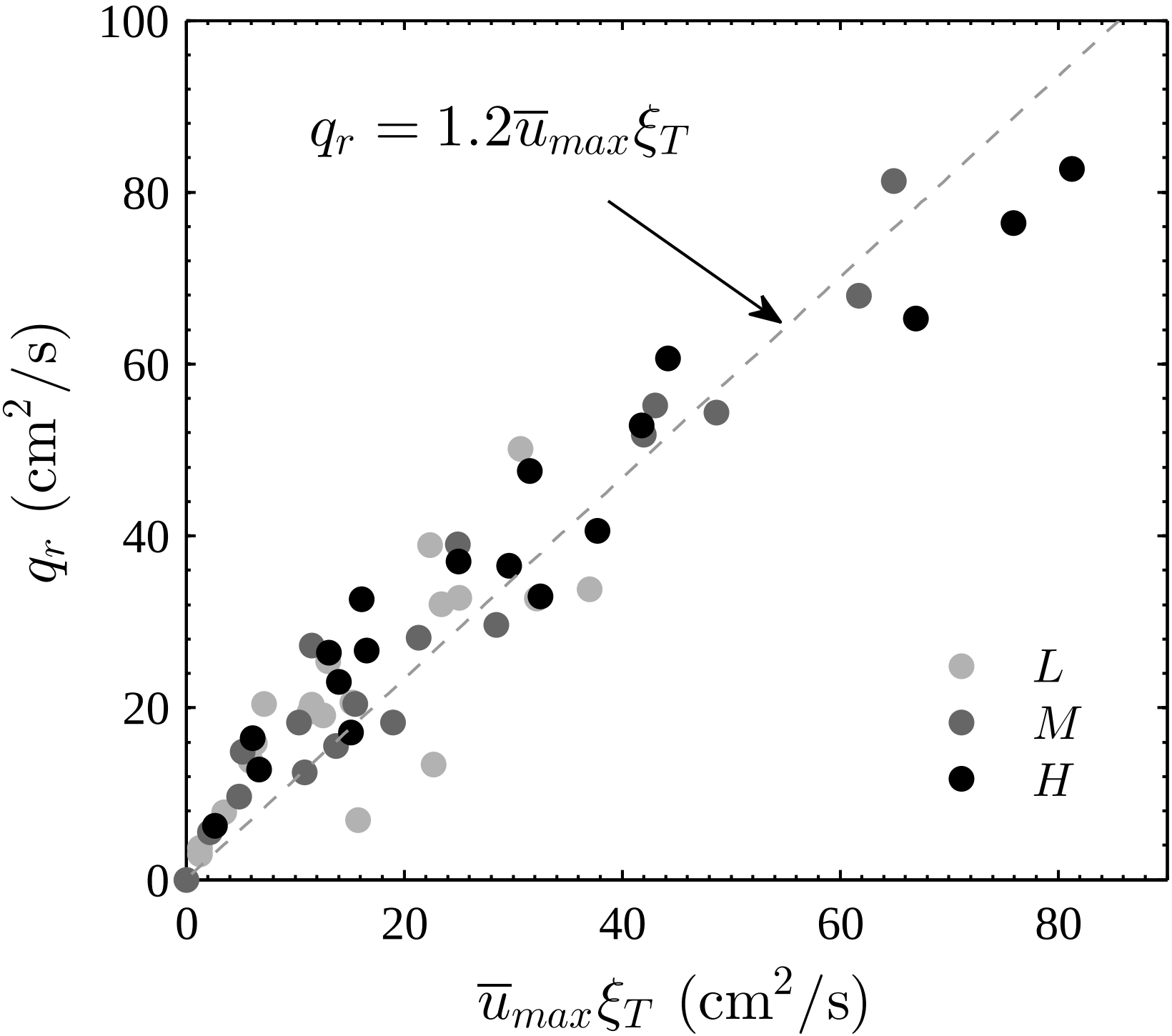
$q_r = 1.2\overline{u}_{max}\xi_T$
q_r (cm^2/s)
$\overline{u}_{max}\xi_T$ (cm^2/s)
0
20
40
60
80
100
L
M
H

Figure 15.

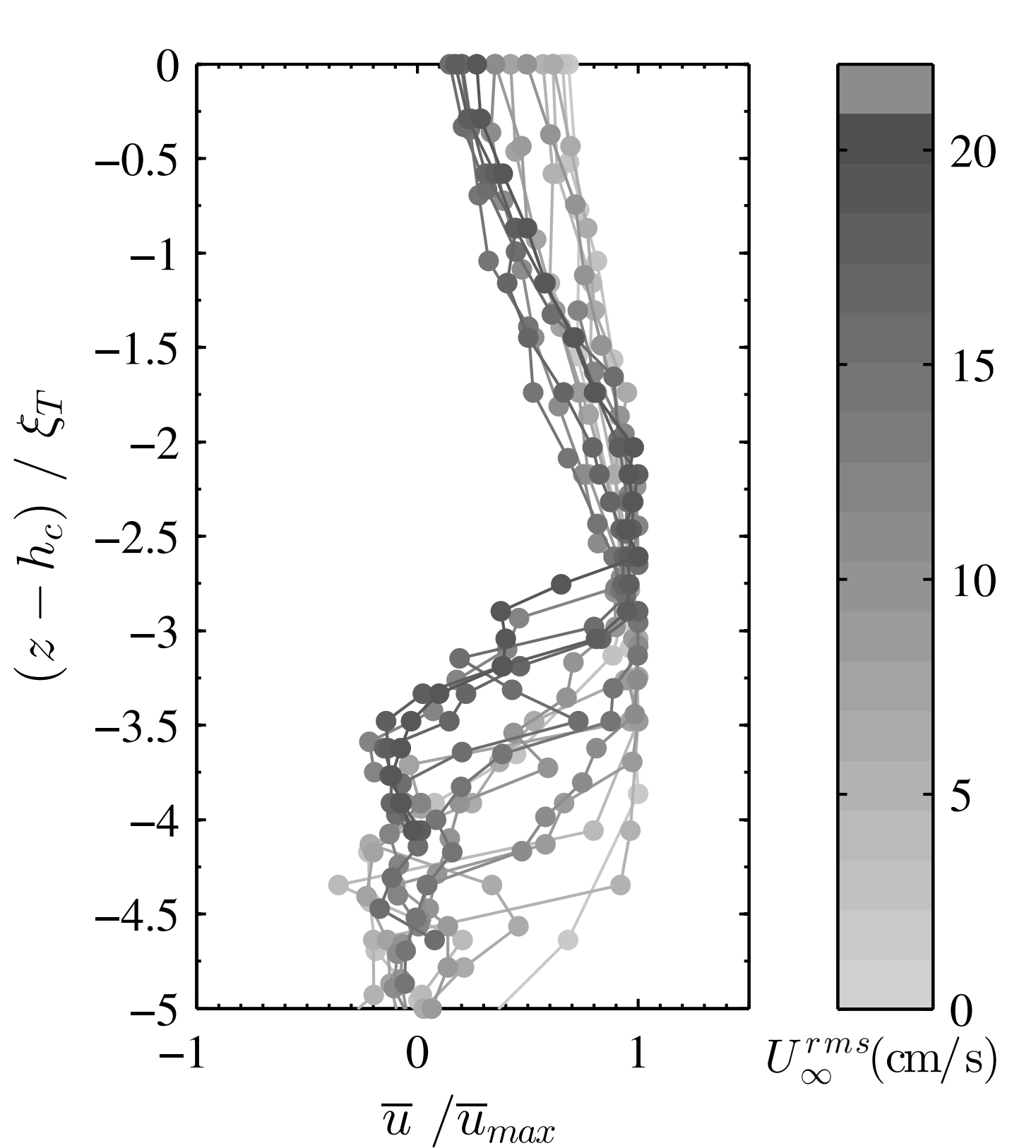
0
−0.5
−1
−1.5
−2
−2.5
−3
−3.5
−4
−4.5
−5
$(z - h_c)\ /\ \xi_T$
−1
0
1
$\overline{u}\ /\overline{u}_{max}$
20
15
10
5
0
U_∞^{rms}(cm/s)

Figure 16.

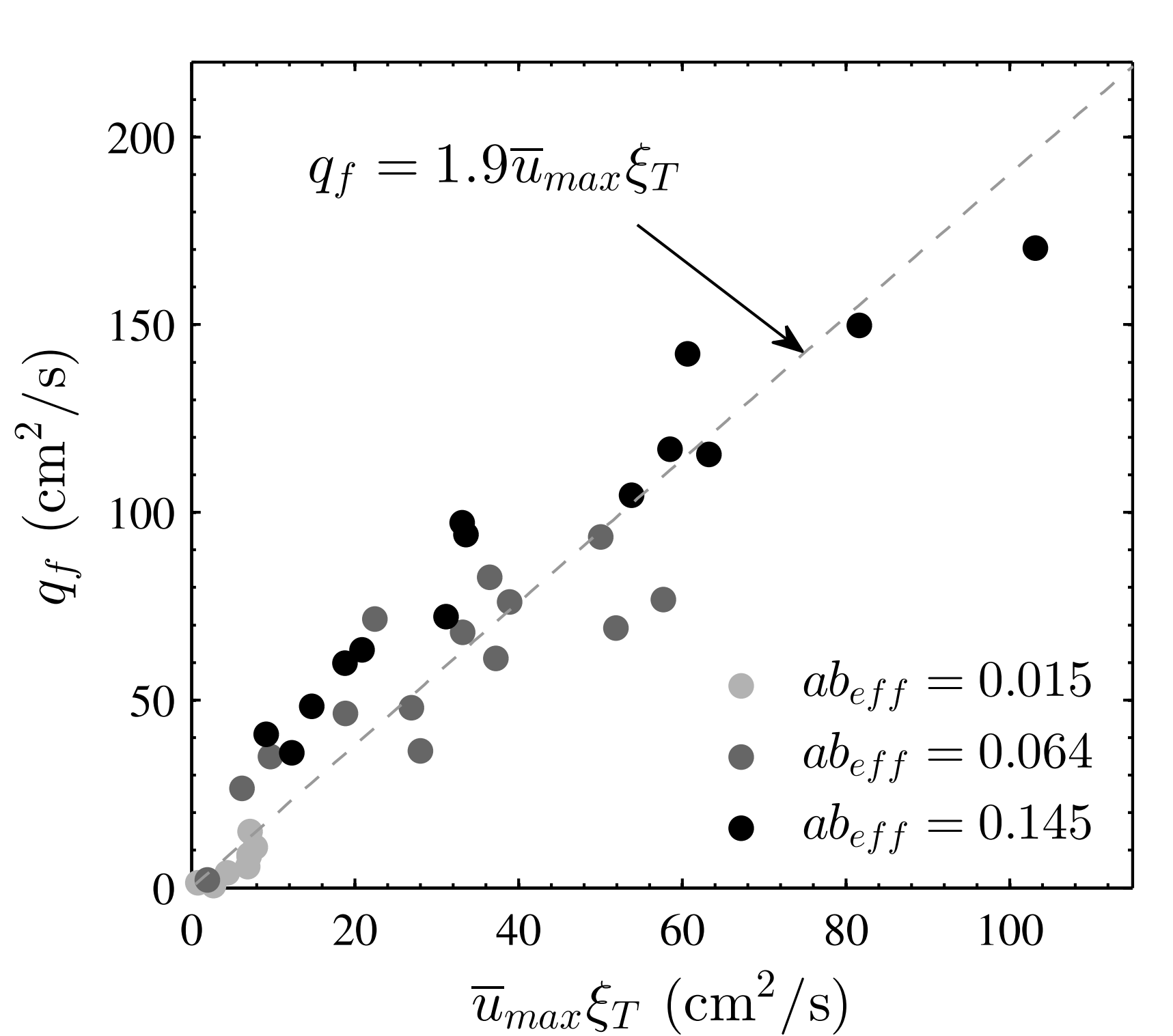
$q_f = 1.9\overline{u}_{max}\xi_T$
$ab_{eff} = 0.015$
$ab_{eff} = 0.064$
$ab_{eff} = 0.145$
q_f (cm^2/s)
$\overline{u}_{max}\xi_T$ (cm^2/s)
0
50
100
150
200
0
20
40
60
80
100